Journal of Computational Physics 345 (2017) 510–527

Contents lists available at ScienceDirect

Journal of Computational Physics

www.elsevier.com/locate/jcp

Numerical investigations of two-phase flow with dynamic capillary pressure in porous media via a moving mesh method

Hong Zhang *, Paul Andries Zegeling

Department of Mathematics, Faculty of Science, Utrecht University, Budapestlaan 6, 3584 CD Utrecht, The Netherlands

ARTICLE INFO

Article history:
Received 14 April 2016
Received in revised form 22 May 2017
Accepted 23 May 2017
Available online 31 May 2017

Keywords:
Two-phase flow equation
Dynamic capillary pressure
Saturation overshoot
Traveling wave
Moving mesh method

ABSTRACT

Motivated by observations of saturation overshoot, this paper investigates numerical modeling of two-phase flow in porous media incorporating dynamic capillary pressure. The effects of the dynamic capillary coefficient, the infiltrating flux rate and the initial and boundary values are systematically studied using a traveling wave ansatz and efficient numerical methods. The traveling wave solutions may exhibit monotonic, non-monotonic or plateau-shaped behavior. Special attention is paid to the non-monotonic profiles. The traveling wave results are confirmed by numerically solving the partial differential equation using an accurate adaptive moving mesh solver. Comparisons between the computed solutions using the Brooks–Corey model and the laboratory measurements of saturation overshoot verify the effectiveness of our approach.

1. Introduction

Since the proposition of the dynamic capillary concept [1–3], the modified Buckley–Leverett equation (MBLE)

$$\frac{\partial u}{\partial t}+\frac{\partial}{\partial x}F(u)=-\frac{\partial}{\partial x}[H(u)\frac{\partial}{\partial x}(p_c(u)-\tau\frac{\partial u}{\partial t})], \tag{1}$$

which models the one-dimensional two-phase flow in porous media, has attracted considerable interest in hydrology and mathematics [4–9]. In the MBLE, the third order mixed derivatives term represents the dynamic capillary pressure effect in the phase pressure difference. With the help of this term, Refs. [6,10–12] successfully captured the non-monotonic saturation profiles found by [13–16].

Different versions of the MBLE have been studied from various points of view. Results on traveling wave (TW) solutions, global existence, phase plane analysis and uniqueness of weak solutions are given in [17,7,18,8,9,19]. Ref. [7] shows that the TW solutions of the MBLE can be described by rarefaction wave, admissible Lax shock and undercompressive shock. In order to capture all these structures accurately, several numerical methods have been proposed in literature. A cell-centered finite difference method and a locally conservative Eulerian–Lagrangian method were proposed in Ref. [20], but it's mentioned that such methods may suffer from instabilities in convection-dominated cases and for large dynamic effects. Van Duijn et al. [7] applied a finite difference method which adopted a minmod slope limiter based on the first order upwind and Richtmyer's schemes. The solutions obtained by this method have good agreement with the TW results. Wang and Kao [21]

* Corresponding author.
E-mail addresses: H.Zhang4@uu.nl (H. Zhang), P.A.Zegeling@uu.nl (P.A. Zegeling).

http://dx.doi.org/10.1016/j.jcp.2017.05.041
0021-9991/

extended the second and third order central schemes to capture the nonclassical solutions of the MBLE. Kao et al. [22] split the MBLE into a high-order linear equation and a nonlinear convective equation, and then integrated the linear equation with a pseudo-spectral method and the nonlinear equation with a Godunov-type central-upwind scheme. The computed solutions demonstrate that the higher-order spatial reconstruction using fifth-order WENO5 scheme gives more accurate numerical solutions. Zegeling [23] investigated the non-monotonic behavior of a simple MBLE with an adaptive moving mesh method, the result shows that for obtaining the same accuracy, the adaptive method needs around a factor of 4 fewer grid points than the uniform grid case.

As the moving mesh method has demonstrated outstanding advantages in tracking shocks or steep wave fronts of other two-phase flow equations [24–26], in the present paper, we will study the solutions of the MBLE using this method. To our best knowledge, the adaptive moving mesh method has not been applied to solve the full MBLE which includes gravity and non-linear diffusion.

The rest of the paper is organized as follows. In Section 2, we outline the derivation of the two-phase flow equation and present some TW analysis. Section 3 introduces a moving mesh method in terms of coordinate transformation. Numerical experiments are presented in Section 4 to show the effectiveness of the proposed method. Section 5 ends with the conclusion.

2. Background

In this section, we first derive the two-phase flow equation and then present some TW results.

2.1. The one-dimensional two-phase flow equation with dynamic capillary pressure term

Here we use the fractional flow formulation to describe two-phase wetting-non-wetting immiscible flow in one dimension. The saturation of each phase is defined as the volumetric fraction of the volume occupied by that phase. Denote the saturation of the wetting phase by u, then for a fully saturated porous medium, the saturation of the non-wetting phase is $1-u$. Let the gravity act in the positive x-direction, for each phase, the Darcy–Buckingham law gives

$$\begin{aligned} v_\alpha &= -\frac{k_{r\alpha}(u)K}{\mu_\alpha}\frac{\partial}{\partial x}(p_\alpha - \rho_\alpha g x) \\ &= -\lambda_\alpha(u)(\frac{\partial p_\alpha}{\partial x} - \rho_\alpha g), \end{aligned} \tag{2}$$

where $\alpha = w, n$ is an index of the wetting and non-wetting phases, K is the intrinsic permeability of the porous medium, g is the gravitational acceleration constant, $k_{r\alpha}(u)$, μ_α, $\lambda_\alpha(u) = \frac{k_{r\alpha}(u)K}{\mu_\alpha}$, p_α, ρ_α and v_α are the relative permeability function, viscosity, mobility, pressure, density and volumetric velocity (flux rate across a unit area) of phase α, respectively.

Define the total velocity $v_T = v_n + v_w$ and fractional flow rate of the wetting phase $f(u) = \frac{\lambda_w(u)}{\lambda_w(u)+\lambda_n(u)}$, then the velocity of the wetting phase can be expressed by

$$v_w = f(u)[v_T + \lambda_n(u)(\frac{\partial(p_n - p_w)}{\partial x} + (\rho_w - \rho_n)g)]. \tag{3}$$

Under non-equilibrium conditions, Stauffer [2], Hassanizadeh and Gray [3], Kalaydjian [27] proposed that the phases pressure difference $p_n - p_w$ can be written as a function of the equilibrium capillary pressure minus the product of the saturation rate of the wetting phase with a dynamic capillary coefficient τ [Pa s]:

$$p_n - p_w = p_c(u) - \tau\frac{\partial u}{\partial t}, \tag{4}$$

where p_c modeling the capillary pressure under equilibrium condition, is a smooth and decreasing function of saturation u, and τ can be explained as a relaxation time. We refer to [4] for a review of experimental work on dynamic effects in the pressure–saturation relationship.

For the wetting phase, the mass conservation equation reads

$$\frac{\partial(\phi\rho_w u)}{\partial t} + \frac{\partial}{\partial x}(\rho_w v_w) = \rho_w F_w, \tag{5}$$

where ϕ is the porosity of the porous medium and F_w is source of wetting phase.

Assuming that ϕ and temperature are constant, the phases are incompressible and neglecting the source term, using (4) and substituting (3) into (5) give the MBLE

$$\frac{\partial u}{\partial t} + \frac{\partial F(u)}{\partial x} = -\frac{\partial}{\partial x}[H(u)\frac{\partial}{\partial x}(p_c(u) - \tau\frac{\partial u}{\partial t})]. \tag{6}$$

In (6) the flux $F(u)$ and the capillary induced diffusion [28] $H(u)$ are given by

$$F(u) = \frac{1}{\phi} f(u)[v_T + \lambda_n(u)(\rho_w - \rho_n)g], \tag{7}$$

$$H(u) = \frac{1}{\phi} \lambda_n(u) f(u). \tag{8}$$

The fractional flow rate $f(u)$ has a characteristic S-shaped graph. When gravity is included, with different values of v_T, the graphs of $F(u)$ are illustrated in Fig. 6 (left) and Fig. 9 (left). Since the saturation in porous media only make sense when $u \in [0, 1]$, in the following we restrict, therefore, $u \in [0, 1]$.

2.2. Traveling waves

Traveling wave solutions of the MBLE have been investigated in Refs. [7,9,18]. For the Riemann problem

$$u(x, 0) = \begin{cases} u_l, & x \le 0, \\ u_r, & x > 0, \end{cases} \tag{9}$$

with different combinations of (u_l, u_r, τ), the MBLE may have different types of solutions, for example, the admissible Lax shock, rarefaction wave and undercompressive shock [7,9,18]. In this section, we follow [7] and study the TW solutions of the MBLE.

To find a TW solution for the MBLE, we introduce the new variable $\eta = x - st$. Substituting $u(\eta)$ into (6) results in a third order ordinary differential equation (ODE)

$$\begin{cases} -su' + [F(u)]' = -[H(u)p_c'(u)u']' - s\tau[H(u)u'']', \\ u(-\infty) = u_l, \quad u(+\infty) = u_r, \quad u_l, u_r \in [0, 1], \\ u'(\pm\infty) = u''(\pm\infty) = 0, \end{cases} \tag{10}$$

where prime denotes differentiation with respect to η, the boundary conditions of the ODE are obtained by the definition of TW solutions. Integrating this equation over $(\eta, +\infty)$ and assuming

$$[H(u)(p_c'(u)u' - s\tau u'')](\pm\infty) = 0, \tag{11}$$

yields the second-order ODE:

$$\begin{cases} -s(u - u_r) + [F(u) - F(u_r)] = -H(u)p_c'(u)u' - s\tau H(u)u'', \\ u(-\infty) = u_l, \quad u(+\infty) = u_r, \end{cases} \tag{12}$$

with s determined by the Rankine–Hugoniot condition

$$s = \frac{F(u_l) - F(u_r)}{u_l - u_r}. \tag{13}$$

When gravity is included into the flux function $F(u)$, Fig. 6 (left) and Fig. 9 (left) show that, with different values of v_T, $F(u)$ may be non-monotone. For simplicity, we only consider the (u_l, u_r) pairs that satisfy $s > 0$.

In (6), when $F(u)$, $H(u)$ and $p_c(u)$ are given by

$$F(u) = \frac{u^2}{u^2 + M(1-u)^2}, \quad H(u) = \epsilon^2, \quad p_c(u) = -\frac{u}{\epsilon}, \tag{14}$$

Van Duijn et al. in Ref. [7] proved that the existence of the TW solution satisfying (12) depends on the values of (u_l, u_r, τ).

When considering (14), we can summarize the results obtained by Ref. [7] as follows. Let u_I be the unique inflection point of the flux function $F(u)$. Consider $u_0 \in [0, u_I)$, then it's proved that there is a constant τ_* such that for all $\tau \in [0, \tau_*]$, there exists a unique solution of (12) connecting $u_l = u_\alpha$ and $u_r = u_0$, where u_α is the unique root of the equation

$$F'(u) = \frac{F(u) - F(u_0)}{u - u_0}. \tag{15}$$

When $\tau > \tau_*$, there exists a unique constant $\bar{u} > u_\alpha$, such that (12) has a unique solution connecting $u_l = \bar{u}$ and $u_r = u_0$. For $u_r = u_0 < u_l = u_B < \bar{u}(\tau)$, the solution of (12) will exist only if $u_B \in (u_0, \underline{u})$, where $\underline{u}$ is the unique root in the interval $(u_0, \bar{u})$ of

$$\frac{F(u) - F(u_0)}{u - u_0} = \frac{F(\bar{u}) - F(u_0)}{\bar{u} - u_0}. \tag{16}$$

When $\tau > \tau_*$ and $u_B \in (\underline{u}, \bar{u})$, there is no TW solution of (12) connecting $u_l = u_B$ and $u_r = u_0$. In this situation, the solution profile is non-monotonic, two TWs are used in succession: one from $u_l = u_B$ to $u_r = \bar{u}$ and one from $u_l = \bar{u}$ to $u_r = u_0$. For any $u_B \in (\underline{u}, \bar{u})$ and $\tau > \tau_*$, there exists a unique solution of (12) such that $u_l = u_B$, $u_r = \bar{u}$.

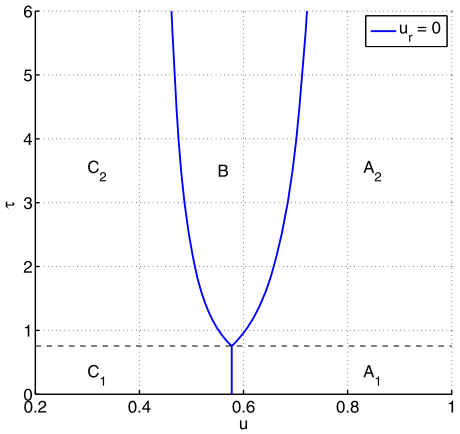

Fig. 1. Bifurcation diagram for the choice (14) with $M = 0.5, \epsilon = 10^{-3}, u_0 = 0$.

Table 1
Results summarized from Ref. [7].

Region	Solution description
$(u_B, \tau) \in A_1$	Rarefaction wave from u_B down to u_α trailing an admissible Lax shock from u_α down to u_0
$(u_B, \tau) \in A_2$	Rarefaction wave from u_B down to $\bar{u}$ trailing an undercompressive shock from $\bar{u}$ down to u_0
$(u_B, \tau) \in B$	An admissible Lax shock from u_B up to $\bar{u}$ (may exhibit oscillations near $u_l = u_B$) trailing an undercompressive shock from $\bar{u}$ down to u_0
$(u_B, \tau) \in C_1$	An admissible Lax shock from u_B down to u_0
$(u_B, \tau) \in C_2$	An admissible Lax shock from u_B down to u_0 (may exhibit oscillations near $u_l = u_B$)

For a given $\bar{u} > u_\alpha$, an algorithm to determine the value of τ is presented in Ref. [7]. This is based on the following concept, invert the function $u(\eta)$ and define the new dependent variable $w(u) = -u'(\eta(u))$, which satisfies

$$s\tau H(u) w w' - H(u) p_c'(u) w = s(u - u_r) - [F(u) - F(u_r)], \tag{17}$$

with boundary condition

$$w(u_r = u_0) = w(u_l = \bar{u}) = 0. \tag{18}$$

The value of τ corresponding to a given $\bar{u}$ can be computed using a shooting method. For more details on this, we refer to [7]. To show the relationship between τ–$\bar{u}$, we take $M = 0.5$, $\epsilon = 10^{-3}$, and plot the bifurcation diagram for $u_0 = 0$ in Fig. 1.

When $u_0 < u_l$ and $u_B > u_0$, the traveling solutions can be classified using the five regions in the bifurcation diagram. The results summarized from Ref. [7] are given in Table 1.

Next we write Eq. (12) as a first order system of ODEs:

$$\begin{cases} u' = v, \\ v' = \dfrac{1}{s\tau H(u)} \big[s(u - u_r) - [F(u) - F(u_r)] - H(u) p_c'(u) v \big]. \end{cases} \tag{19}$$

When $u_l \neq u_\alpha$, $u_r = u_0$, the ODE system has three equilibria:

$$(u, v) = (u_0, 0), \quad (u, v) = (\underline{u}, 0), \quad (u, v) = (\bar{u}, 0). \tag{20}$$

Since the magnitude of $H'(u)$ is usually very small (in Eq. (14) $H'(u) = 0$, in Example 6 $H'(u) = \mathcal{O}(10^{-7})$), thus an approximation to the Jacobian of (19) reads

$$A = \begin{bmatrix} 0 & 1 \\ \frac{s - F'(u)}{s\tau H(u)} & -\frac{p_c'(u)}{s\tau} \end{bmatrix}, \tag{21}$$

and has eigenvalues

$$\lambda_\pm = \frac{1}{2s\tau} [-p_c'(u) \pm \sqrt{(p_c'(u))^2 - 4s\tau \frac{F'(u) - s}{H(u)}}]. \tag{22}$$

From this we can get the classification of the three equilibria. The outside two equilibria $(u_0, 0)$ and $(\bar{u}, 0)$ are saddles and the middle equilibrium $(\underline{u}, 0)$ is either an unstable node or a spiral since $F'(u) > s$. When $\underline{u} < u_B < \bar{u}$ (or $u_0 < u_B < \underline{u}$), consider a TW connecting $u_l = u_B$ and $u_r = \bar{u}$ (or $u_r = u_0$) and the wave speed is

$$s = \frac{F(u_l) - F(u_r)}{u_l - u_r}. \tag{23}$$

When using (22) and $\tau > \tau_s = \frac{H(u_l)p_c'(u_l)^2}{4s(F'(u_l)-s)}$, the equilibrium $(u_B, 0)$ is a spiral.

Remark. When $u_l < u_0 < 1$ and $0 < u_B < u_0$, the TW solutions of (12) can be obtained in a similar way. In this case, the roles of $\bar{u}$ and $\underline{u}$ have been switched: $\underline{u}$ is denoted as the basin height, $\bar{u}$ is the unique root in the interval $(\underline{u}, u_0)$ of

$$\frac{F(u) - F(u_0)}{u - u_0} = \frac{F(\underline{u}) - F(u_0)}{\underline{u} - u_0}. \tag{24}$$

The boundary condition (18) is also replaced by

$$w(u_r = u_0) = w(u_l = \underline{u}) = 0. \tag{25}$$

3. The adaptive moving mesh method

With the appearance of the non-monotonic profiles as mentioned in the previous section, an ideal mesh used in the simulation should be able to capture the overshoot of the saturation on the wetting front. When the initial saturation u_0 is very small, the solution of ODE (17) may have a large magnitude (see Fig. 12 (right)), which means a sufficiently dense grid should be used near the wetting front to resolve the sharp profile. Note that, the solution is smooth in the region far away from the wetting front, thus a coarse mesh could be used in this region. Based on the above observations, we choose an adaptive moving mesh method [29,30] to distribute the grid points dynamically in accordance with the evolution of the solution.

Adaptive moving mesh method continuously repositions a fixed number of grid points according to a monitor function ω, so that the resolution in particular locations of the computational domain is improved. Generally, to apply the moving mesh method, three steps have to be taken.

1. Transform the PDE from the physical domain to a computational domain.
2. Define the adaptive mesh transformation.
3. Discretize the coupled system of PDEs in the spatial direction, then compute the numerical solution by applying a suitable time-integrator to the semi-discrete system.

3.1. Transformation of the two-phase flow equation

Let x and ξ denote the physical and computational coordinates. Without lose of generality, x is assumed to be in the interval $\Omega_p = [x_l, x_r]$ and $\xi \in \Omega_c = [0, 1]$. A general coordinate transformation between x and ξ is given by

$$x = x(\xi, t), \quad \xi \in [0, 1], t \in [0, T], \tag{26}$$

with

$$x(0, t) = x_l, \quad x(1, t) = x_r, \tag{27}$$

where t denotes time. Let $u_t = \frac{\partial u}{\partial t}$, $u_x = \frac{\partial u}{\partial x}$, $u_\xi = \frac{\partial u}{\partial \xi}$ and $\dot{x} = \frac{\mathrm{d}x}{\mathrm{d}t}$, in the new coordinate, using the total differential $\dot{u} = \frac{\mathrm{d}u}{\mathrm{d}t} = u_t + u_x\dot{x}$, the physical PDE is transformed to its Lagrangian form

$$(\mathcal{I} - \tau \frac{\partial}{\partial x} H(u) \frac{\partial}{\partial x})(\dot{u} - u_x\dot{x}) + \frac{\partial}{\partial x} F(u) + \frac{\partial}{\partial x}[H(u) \frac{\partial}{\partial x} p_c(u)] = 0, \tag{28}$$

where $\mathcal{I}$ is the identity operator. In the next section the transformed PDE will be coupled with a moving mesh PDE (MMPDE) which defines the mesh movement and the monitor function.

3.2. Mesh transformation with smoothing

Given a uniform computational mesh with space step $\Delta\xi = \frac{1}{N}$, $\xi_i = \frac{i}{N}$, $i = 0, 1, \cdots, N$, an adaptive physical mesh x_i, $i = 0, 1, 2, \cdots, N$ is built to equidistribute a specified monitor function ω. In continuous form, the equidistribution principle (EP) [31] of the mesh can be expressed as

$$\int_{x_{i-1}}^{x_i} \omega \mathrm{d}x = \int_{x_i}^{x_{i+1}} \omega \mathrm{d}x = c, \quad 1 \le i \le N-1, \tag{29}$$

or in discrete form

$$\omega_{i-1}\Delta x_{i-1} = \omega_i \Delta x_i = c, \quad 1 \le i \le N-1, \tag{30}$$

where $\Delta x_i = x_{i+1} - x_i$ is the local grid spacing, ω_i is a discrete approximation of the monitor function ω in the grid interval $[x_i, x_{i+1}]$, and c is a constant determined from

$$\int_{\Omega_p} \omega \mathrm{d}x = \sum_{i=1}^{N} \int_{x_{i-1}}^{x_i} \omega \mathrm{d}x = Nc. \tag{31}$$

The monitor function ω is chosen to cluster mesh points in regions where more accuracy is needed, so it's usually taken to be some measure of the error estimated from the discrete solution. As is often seen in literature, for a scalar solution u, a popular choice for controlling grid concentration is based on the arc-length type monitor

$$\omega = \sqrt{1 + \alpha |u_x|^2}, \tag{32}$$

where the parameter α controls the amount of adaptivity, in this work we set $\alpha = 1$. The choice of the 'optimal' monitor function according to interpolation error estimates has been discussed in Ref. [32]. In this work, we consider a smoothed monitor function proposed by Ref. [33]

$$\omega = (1-\beta)\alpha(u) + \beta |u_\xi|^{\frac{1}{m}}, \tag{33}$$

where the intensity controlling parameter $\alpha(u)$ is defined as

$$\alpha(u) = \frac{1}{|\Omega_c|} \int_{\Omega_c} |u_\xi|^{\frac{1}{m}} \mathrm{d}\xi. \tag{34}$$

In (33), the critical regions are identified by the computational derivative u_ξ, which is smoother than the physical derivative u_x. The function $\alpha(u) > 0$ averages the derivative u_ξ, resulting in an adaptive smoothed monitor function. In this work, we take $m = 1$, this choice is verified to be robust and efficient in Refs. [33,34].

Following the approach from [35], we can derive that

$$\begin{aligned} \int_{\Omega_c} \omega \mathrm{d}\xi &= \int_{\Omega_c} [\frac{1-\beta}{|\Omega_c|} \int_{\Omega_c} |u_\xi|^{\frac{1}{m}} \mathrm{d}\xi + \beta |u_\xi|^{\frac{1}{m}}] \mathrm{d}\xi \\ &= \int_{\Omega_c} [(1-\beta)|u_\xi|^{\frac{1}{m}} + \beta |u_\xi|^{\frac{1}{m}}] \mathrm{d}\xi \\ &= \int_{\Omega_c} |u_\xi|^{\frac{1}{m}} \mathrm{d}\xi, \end{aligned} \tag{35}$$

thus β is indeed the ratio of points in the critical areas. In this paper we choose $\beta = 0.9$, which means approximately 90% grid points are distributed in the critical regions [35].

The accuracy of the spatial derivative approximations and stiffness of the system after the space discretization are largely influenced by the regularity of the mesh. To equidistribute the monitor function, we adopt a MMPDE with smoothing [29,30],

$$\begin{cases} \dfrac{\partial}{\partial \xi}\left(\dfrac{\dot{\tilde{n}}}{\omega}\right) = -\dfrac{1}{\tau_s}\dfrac{\partial}{\partial \xi}\left(\dfrac{\tilde{n}}{\omega}\right), \\ \tilde{n} = [\mathcal{I} - \sigma_s(\sigma_s+1)(\Delta\xi)^2 \dfrac{\partial^2}{\partial \xi^2}]n, \end{cases} \tag{36}$$

where σ_s and τ_s are the spatial and temporal smoothing parameters, $n = \frac{1}{x_\xi}$ is the point concentration, $\Delta\xi$ is the space step of the computational domain after discretization.

Refs. [29,30] show that this smoothed MMPDE has the following properties

1. No node-crossing: $J = x_\xi > 0$, in discrete version it reads, $\Delta x_i(t) > 0$, $\forall t \in [0, T]$.

2. Local quasi-uniformity: $|\frac{x_{\xi\xi}}{x_\xi}| \le \frac{1}{\sqrt{\sigma(\sigma+1)}\Delta\xi}$ with discretized version:

$$\frac{\sigma}{\sigma+1} \le \frac{\Delta x_{i+1}(t)}{\Delta x_i(t)} \le \frac{\sigma+1}{\sigma}, \quad \forall t \in [0,T]. \tag{37}$$

3. When $\sigma_s = \tau_s = 0$ (no smoothing), (36) fulfills the basic equidistribution principle of the monitor function:

$$\omega x_\xi = \text{constant}, \quad \forall t \in [0,T], \tag{38}$$

in discretized form it reads

$$\omega_i \Delta x_i = \text{constant}, \quad \forall t \in [0,T]. \tag{39}$$

For the choice of the parameters τ_s and σ_s, we follow the suggestions in Ref. [29]. In practice, the choice of the temporal smoothing parameter depends on the timescale in the model: $\tau_s = 10^{-3}\times$ 'timescale in PDE model'. The spatial smoothing parameter σ_s can be taken as $\sigma_s = \mathcal{O}(1)$. In Section 4, for all numerical experiments using the moving mesh method, we set $\tau_s = 10^{-3} \times T_{end}$ and $\sigma_s = 2$.

3.3. Discretization of the coupled PDEs

We employ a finite difference method to discretize the coupled system. Applying the second order centered finite difference scheme in space direction to (36) yields

$$\begin{cases} \dfrac{[\mathcal{I}-\sigma_s(\sigma_s+1)\delta_{xx}](\dot{x}_{i+1}-\dot{x}_i)}{\omega_{i+1/2}(x_{i+1}-x_i)^2} - \dfrac{[\mathcal{I}-\sigma_s(\sigma_s+1)\delta_{xx}](\dot{x}_i-\dot{x}_{i-1})}{\omega_{i-1/2}(x_i-x_{i-1})^2} = \\ \qquad \dfrac{1}{\tau_s}\left[\dfrac{[\mathcal{I}-\sigma_s(\sigma_s+1)\delta_{xx}]\frac{1}{x_{i+1}-x_i}}{\omega_{i+1/2}} - \dfrac{[\mathcal{I}-\sigma_s(\sigma_s+1)\delta_{xx}]\frac{1}{x_i-x_{i-1}}}{\omega_{i-1/2}}\right], \quad i=2,3,\cdots,N-2, \\ \dot{x}_{i+1}-2\dot{x}_i+\dot{x}_{i-1}=0, \quad i=1,N-1, \\ \dot{x}_0=\dot{x}_N=0, \end{cases} \tag{40}$$

where δ_{xx} is the second-order difference operator and $\omega_{i+1/2} = (1-\beta)\alpha(u) + \beta|\frac{u_{i+1}-u_i}{\Delta\xi}|$. The derivative of the point concentration appears in (36) is discretized as

$$\dot{n}_i = -\frac{\dot{x}_{i+1}-\dot{x}_i}{(x_{i+1}-x_i)^2}, \quad i=0,1,\cdots,N-1. \tag{41}$$

The transformed physical PDE (28) is discretized in the same way. Following the method-of-lines approach, the time-integration of the resulting coupled semi-discretized system is solved using the BDF integrator ode15i of Matlab [36].

4. Numerical experiments

In this section, we present some numerical results obtained by the moving mesh method described in the previous section. First we show the convergence order of the method. Then three examples are adopted to show the accuracy and features of the moving mesh method. The fourth and fifth examples study the effects of the flux rate and initial saturation by taking gravity into account, the last one solves the full equation by utilizing the Brooks–Corey model [37].

4.1. Convergence order

To test the convergence order of the moving mesh method, we first consider a linear equation whose solution is smooth:

$$\begin{cases} \dfrac{\partial u}{\partial t} - \epsilon\dfrac{\partial^2 u}{\partial x^2} - \tau\epsilon^2\dfrac{\partial^3 u}{\partial x^2\partial t} = 0, \quad x\in[0,1] \\ u(x;0) = \cos(2\pi x), \\ u(\partial\Omega;t) = u_{ex}(\partial\Omega;t). \end{cases} \tag{42}$$

The exact solution of (42) is $u_{ex}(x;t) = \exp(-\frac{4\pi^2\epsilon}{4\pi^2\tau\epsilon^2+1}t)\cos(2\pi x)$. Choosing $\epsilon = 0.01, \tau = 1$, the corresponding errors and orders for $N = 32, 64, 128, 256$ are presented in Fig. 2 and Table 2 from which a second-order rate of convergence is observed.

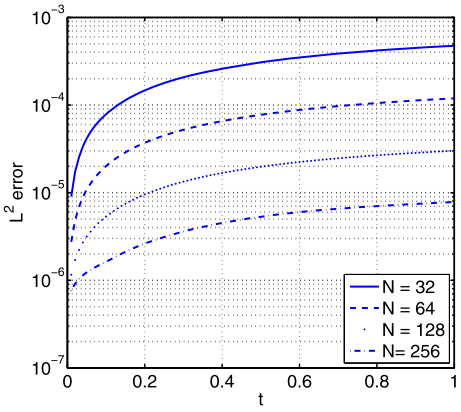

Fig. 2. Evolution of numerical errors for Eq. (42) obtained using grid numbers $N = 32, 64, 128, 256$, with $\epsilon = 0.01$, $\tau = 1$, $t \in [0, 1]$.

Table 2
Numerical Errors and convergence orders for Eq. (42) with $\epsilon = 0.01, \tau = 1$ at $T = 1$.

Mesh size	L^2 error	L^2 order	L^∞ error	L^∞ order
$N = 32$	4.7508e−04	–	8.4972e−04	–
$N = 64$	1.1916e−04	1.9953	2.1311e−04	1.9954
$N = 128$	3.0000e−05	1.9851	5.3868e−05	1.9841
$N = 256$	7.8219e−06	1.9941	1.4036e−05	1.9403

Table 3
Traveling wave results for Example 1, 2 and 3.

	u_B	u_0	τ	τ_*	τ_s	u_α	$\underline{u}$	$\bar{u}$	Wave description
Example 1	0.25	0.85	3.5	0.6826	0.4495	0.2151	0.1036	0.3155	Non-monotone basin
	0.85	0	3.5	0.7545	–	0.5774	0.4804	0.6938	Monotone plateau
Example 2	0.25	0.66	5	1.0560	1.0775	0.2702	0.2027	0.3353	Non-monotone basin
	0.66	0	5	0.7545	2.5023	0.5774	0.4674	0.7130	Non-monotone plateau
Example 3	0.25	0.52	5	3.0723	–	0.3246	0.3109	0.3382	Monotone basin
	0.52	0	5	0.7545	0.4154	0.5774	0.4674	0.7130	Non-monotone plateau

4.2. The accuracy of the moving mesh method

In this part, we use three examples to test the accuracy of the moving mesh method. Examples 1, 2 and 3 are modifications of the test cases in Ref. [22].

Consider $F(u), H(u)$ and $p_c(u)$ given in (14) with $M = 0.5, \epsilon = 10^{-3}$ and initial condition

$$u(x,0) = \begin{cases} u_1, & x \in [0, 0.75], \\ u_2, & x \in (0.75, 2.25), \\ 0, & x \in [2.25, 3]. \end{cases} \tag{43}$$

With different combinations of (u_B, u_0, τ), the TW results obtained from Section 2.2 are shown in Table 3. For this problem, we set the final time $T = 0.5$.

Example 1. $\tau = 3.5, u_1 = 0.25, u_2 = 0.85$.

In the left part of the initial condition, we have $u_B = u_1$, $u_0 = u_2$, Table 3 shows $\tau > \tau_s > \tau_*$ and $\underline{u} < u_B = u_1 < \bar{u}$, thus the left part of the solution consists of an admissible Lax shock from u_B down to $\underline{u}$ (with oscillations near u_B) and an undercompressive shock from $\underline{u}$ up to u_0. In the right part, $u_0 = 0$, since $u_B = u_2 > \bar{u}$ and $\tau > \tau_*$, the right part of the solution consists of a rarefaction wave from u_B down to $\bar{u}$ and an undercompressive shock from $\bar{u}$ down to u_0. In the following, the left and right parts of the solution are called as non-monotone basin and monotone plateau, respectively. The basin height is $\underline{u} = 0.1036$ and the plateau height is $\bar{u} = 0.6938$.

Fig. 3 shows the computed results obtained by the moving mesh method (monitor (32) with $N = 200$, monitor (33) with $N = 200, 400, 800$) and uniform grids ($N = 2000, 4000, 8000$). Fig. 3 (top left) clearly shows that the solution includes a non-monotone basin in the left part and a monotone plateau in the right part. Fig. 3 (top right) plots the opposite slopes

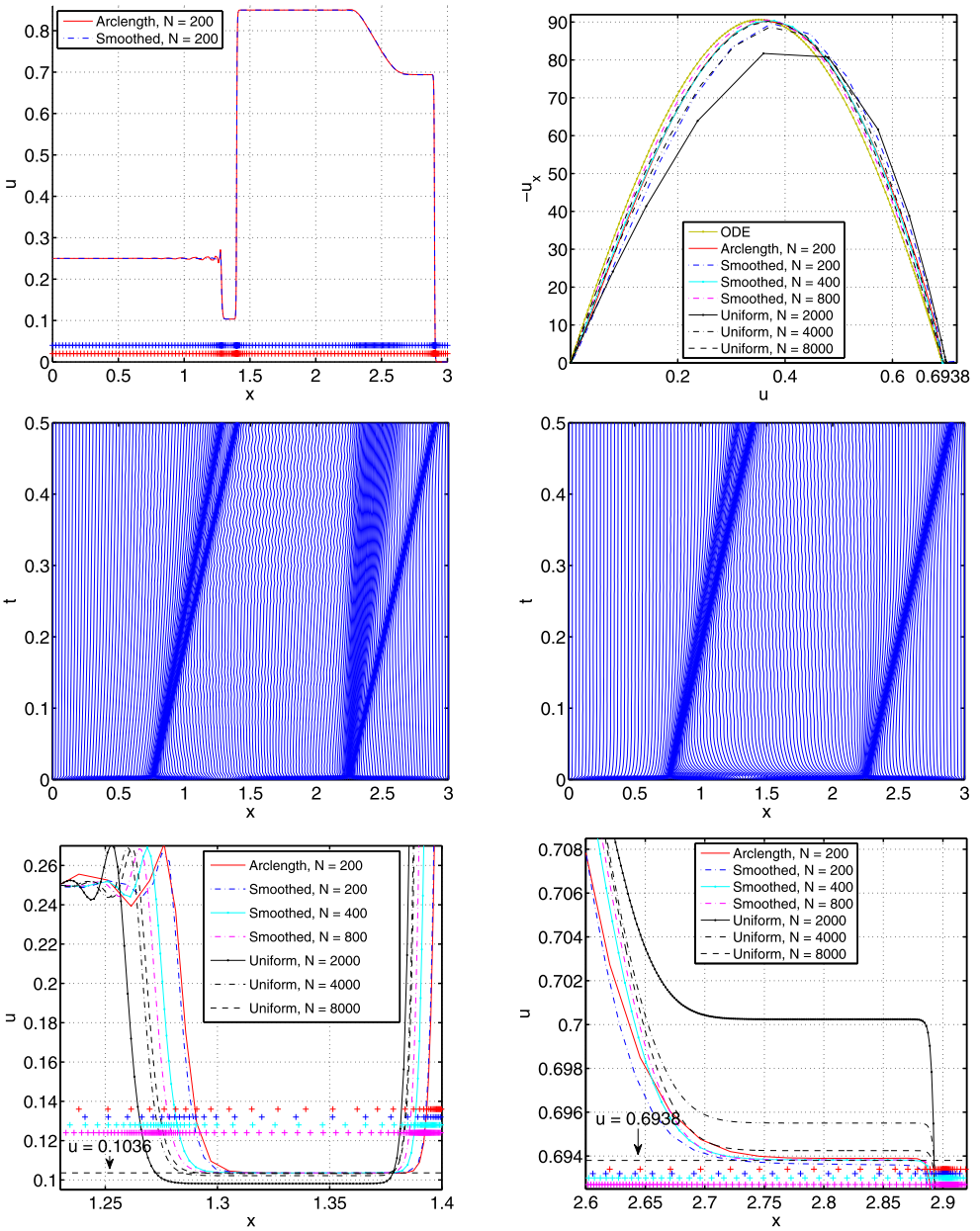

Fig. 3. Example 1: solutions computed using the moving mesh method (top left); values of $-u_x$ at the right boundary of the plateau (top right); grid trajectories using the smoothed monitor function (middle left) and the arc-length monitor function (middle right) with $N = 200$; close-up of the basin area (bottom left); close-up of the plateau area (bottom right).

$(-u_x)$ at the boundary of the right undercompressive shock. The reference slopes are obtained by solving ODE (17) with the built-in function ode15i in Mablab. The slopes computed by the moving mesh method using the smoothed monitor (33) with $N = 200, 400, 800$ are more accurate than those obtained by the uniform grids with $N = 2000, 4000, 8000$, respectively. The grid trajectories produced by the smoothed monitor (33) clearly illustrate the evolution of the solutions. As can be seen, the smoothed monitor attracts more grid points in the rarefaction fan area than the arc-length monitor, while the arc-length monitor attracts more grid points near the steep shocks. Therefore, the slope computed using the arc-length monitor is slightly more accurate than the one using the smoothed monitor.

In order to check the accuracy of the moving mesh method, we present the details of the critical areas (basin and plateau) in Fig. 3 (bottom). The heights of the basin and plateau computed with the moving mesh method ($N = 200, 400, 800$) are more accurate than the heights obtained using a uniform grid with $N = 2000, 4000$ or even 8000. Although the arc-length monitor results in more accurate basin and plateau heights than the smoothed monitor, the accuracy near the admissible Lax shocks is lower as a result of fewer grid points near smooth parts.

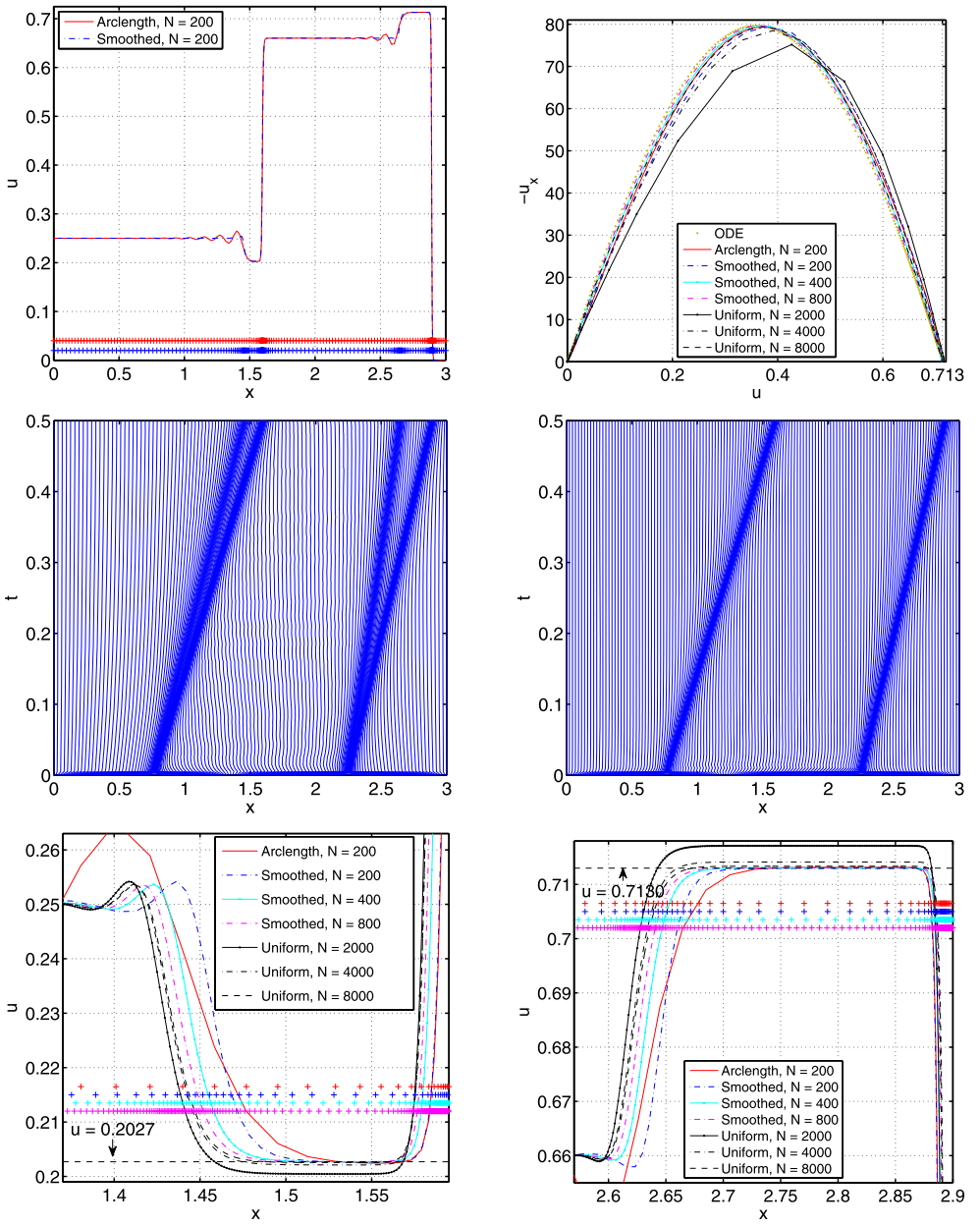

Fig. 4. Example 2: solutions computed using the moving mesh method (top left); values of $-u_x$ at the right boundary of the plateau (top right); grid trajectories using the smoothed monitor function (middle left) and the arc-length monitor function (middle right) with $N = 200$; close-up of the basin area (bottom left); close-up of the plateau area (bottom right).

Example 2. $\tau = 5, u_1 = 0.25, u_2 = 0.66$.

For the second example, u_1 is the same as that in Example 1, u_2 is decreased form 0.85 to 0.66 and τ is increased to 5. Table 3 shows that this combination results in a non-monotone basin of height $\underline{u} = 0.2027$ in the left part and a non-monotone plateau of height $\bar{u} = 0.7130$ in the right part. In the left part, as a result of the decrease in u_2, the height of the basin is higher than the one in Example 1 and the amplitude of the oscillations becomes smaller. In the right part, since $\underline{u} < u_B = u_2 < \bar{u}$ and $\tau > \tau_s > \tau_*$, we obtain a non-monotone plateau which is higher than the one in Example 1. Because u_B is a spiral, a slight oscillation appears near u_B.

Once again, near the admissible Lax shocks, the smoothed monitor performs better than the arc-length monitor as it attracts more grid points near these parts. The moving mesh method leads to much more accurate slopes, plateau and basin heights than the uniform grid method, see Fig. 4.

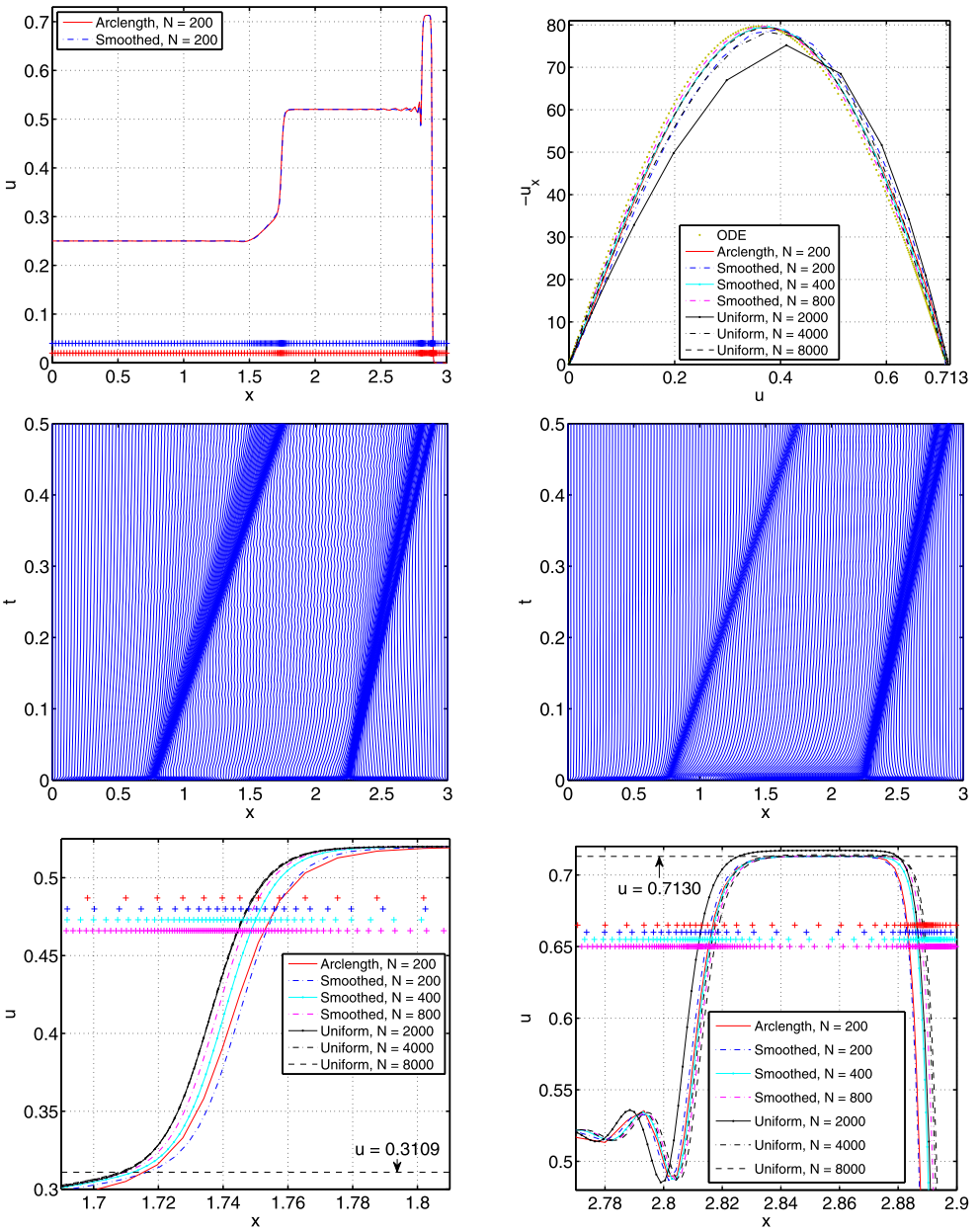

Fig. 5. Example 3: solutions computed using the moving mesh method (top left); values of $-u_x$ at the right boundary of the plateau (top right); grid trajectories using the smoothed monitor function (middle left) and the arc-length monitor function (middle right) with $N = 200$; close-up of the basin area (bottom left); close-up of the plateau area (bottom right).

Example 3. $\tau = 5, u_1 = 0.25, u_2 = 0.52$.

In the third example, a smaller value of u_2 is used. In the left part, $u_B = u_1 < \underline{u}$, therefore the solution has a monotone basin area. Note that, since we only computed to $t = 0.5$, instead of a horizontal basin, only a turning point appears near $\underline{u} = 0.3109$. In the right part, $\underline{u} < u_B < \bar{u}$, $\tau > \tau_* > \tau_s$, hence $(u_B, 0)$ is a spiral of the ODE system (19), consequently oscillations appear near $u_B = u_2$. As in Examples 1 and 2, the plateau heights and slopes obtained by the moving mesh method are more accurate than the uniform grid method, see Fig. 5.

4.3. Influence of the flux rate and the initial saturation

In Example 1, 2 and 3, the effect of the gravity has been neglected. In this section, we take the gravity into account to study the influences of flux rate and initial saturation. Since the smoothed monitor function has a better balance between

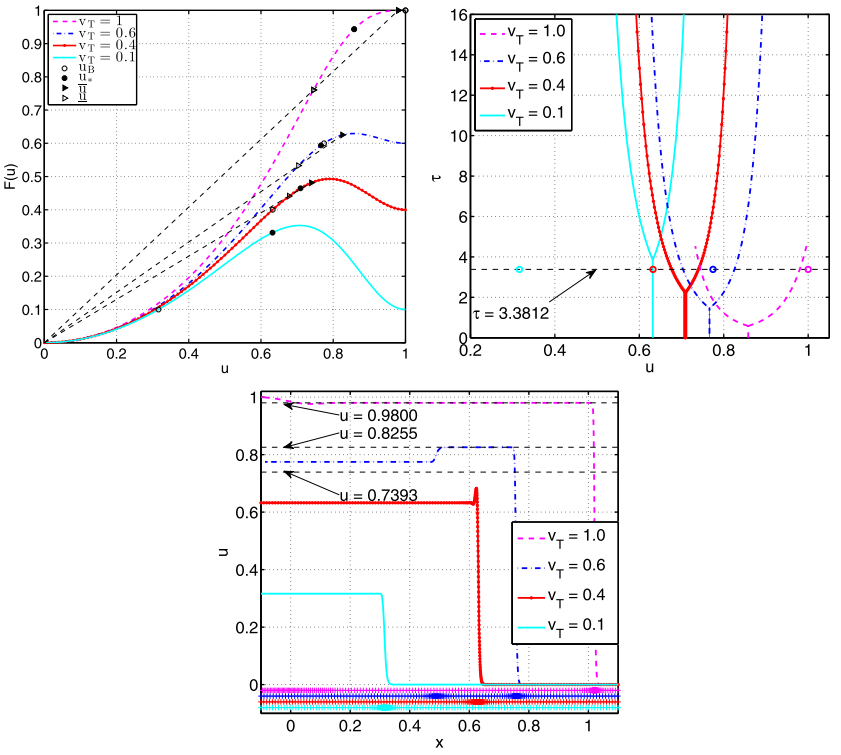

Fig. 6. Flux functions (left), bifurcation diagrams (center) and numerical solutions (right) for different values of v_T.

the smooth and the steep regions than the arc-length monitor function, in the Example 4 and Example 5, we will only consider the smoothed monitor function with $N = 200$.

Consider $H(u)$ and $p_c(u)$ as in (14) with the flux function $F(u)$ replaced by

$$F(u) = \frac{u^2}{u^2 + M(1-u)^2}[v_T + C(1-u)^2], \tag{44}$$

where $\epsilon = 10^{-3}$, $M = 10$, and $C = 10$ is a positive constant that accounts for gravity. The initial condition is

$$u(x, 0) = u_0 + 0.5(u_B - u_0)(1.0 - \tanh(200x)), \quad x \in [-0.1, 1.1]. \tag{45}$$

Example 4. $\tau = 3.3812$, $v_T = 1.0, 0.6, 0.4, 0.1$, $u_0 = 0$, $T = 1$.

In Ref. [16], DiCarlo carried out a series of experiments with different infiltrating fluxes. At the highest (2.0×10^{-3} [m s^{-1}]) and lowest (1.32×10^{-7} [m s^{-1}]) fluxes, the profiles are monotonic and no saturation overshoot is observed. For the intermediate fluxes which exhibit saturation overshoot, as flux decreases both the tip and tail saturations decrease continuously. In this example, we use the simplified gravity model to show how solution varies with the change of flux.

Next we fix the initial saturation $u_0 = 0$ and consider different values of v_T. The flux function $F(u)$ corresponding to v_T are plotted in Fig. 6 (left). As can be seen, when $v_T = 1.0$, the flux function is strictly increasing, when v_T is smaller, the flux function becomes non-monotonic, and the value of u_α becomes lower and results in different bifurcation diagrams. Fig. 6 (center) shows that the value of τ_* increases with decreasing v_T. By solving $F(u) = v_T$, the boundary saturation u_B corresponding to different v_T can be defined. For $\tau = 3.3812$, the TW results are given in Table 4.

When $v_T = 1$, we have $\tau > \tau_*$ and $u_B > \bar{u}(\tau)$. Thus u_B and u_0 are connected by a rarefaction wave from u_B down to $\bar{u}$ trailing an undercompressive shock from $\bar{u}$ down to u_0. When $v_T = 0.6$, we have $\underline{u}(\tau) < u_B < \bar{u}(\tau)$, and therefore a non-monotone plateau of height $\bar{u} = 0.8255$ exists. When $v_T = 0.4$, we have $u_B < \underline{u}$ and $\tau_s < \tau < \tau_*$, hence u_B is a spiral point: there exists an admissible Lax shock connecting u_B and u_0 with oscillations near u_B. When $v_T = 0.1$, $u_B < u_\alpha$ and $\tau < \tau_*$, this combination results in a monotonic profile. The numerical solutions are plotted in Fig. 6 (right). The computed profiles have good agreement with the TW results.

Example 5. $\tau = 2.13$, $v_T = 0.6$, $u_B = 0.75$, $u_0 = 0, 0.1, 0.2, 0.25$, $T = 1$.

Table 4
Traveling wave results for different values of v_T with $\tau = 3.3812$, $u_0 = 0$.

v_T	u_B	u_α	τ_*	τ_s	$\underline{u}(\tau)$	$\bar{u}(\tau)$	Wave description
1.0	1.0000	0.8580	0.5848	–	0.7452	0.9800	Monotone plateau
0.6	0.7746	0.7662	1.4633	2.3406	0.7035	0.8255	Non-monotone plateau
0.4	0.6325	0.7093	2.2330	1.1512	0.6779	0.7393	Non-monotone overshoot
0.1	0.3162	0.6318	3.8537	2.6097	–	–	Monotone, no plateau

Table 5
Traveling wave results for different values of u_0 with $\tau = 2.13$, $u_B = 0.75$.

u_0	u_α	τ_*	τ_s	$\underline{u}(\tau)$	$\bar{u}(\tau)$	Wave description
0.00	0.7662	1.4633	2.0371	0.7354	0.7961	Non-monotone plateau
0.10	0.7519	1.6312	4.0993	0.7320	0.7714	Non-monotone plateau
0.20	0.7358	1.9688	–	0.7306	0.7410	Monotone plateau
0.25	0.7268	2.2537	–	–	–	Monotone, no plateau

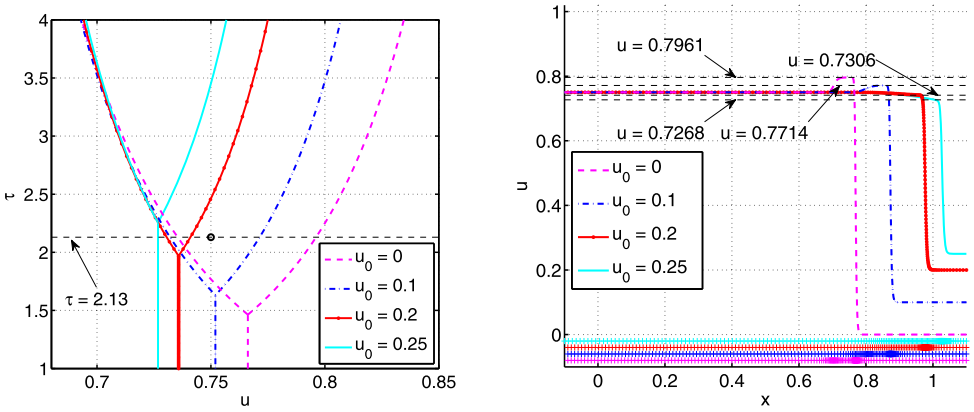

Fig. 7. Bifurcation diagrams (left) and numerical solutions (right) for different values of u_0.

The laboratory experiments in Ref. [16] also show that saturation overshoot decreases quickly with increasing initial water saturation. In this example, we study the influence of the initial saturation u_0.

In Fig. 7 (left) the bifurcation diagrams for various values of u_0 are presented. Choosing $u_B = 0.75$, $\tau = 2.13$, the TW results are presented in Table 5. When $u_0 = 0$ and 0.1, since $\underline{u} < u_B < \bar{u}$ and $\tau > \tau_*$, u_B and u_0 are connected by non-monotone plateaus. The plateau height of $u_0 = 0$ is higher than that of $u_0 = 0.1$. When $u_0 = 0.2$, we have $u_B > \bar{u}$, therefore there exists a rarefaction wave from u_B down to $\bar{u}$ trailing an undercompressive shock from $\bar{u}$ down to u_0. The plateau height $\bar{u}$ is lower than $u_0 = 0$ and 0.1. When $u_r = 0.25$, since $\tau = 2.13$ is smaller than $\tau_* = 2.2537$, we have an admissible Lax shock connecting u_B and u_0. The turning point is $u_\alpha = 0.7268$.

In Fig. 7 (right), we present the numerical solutions. As can be seen, the computed plateau heights and the turning points agree well with those in Table 5. The grids plotted in the lower part of the figure clearly indicate the critical regions of the solutions.

4.4. Numerical solutions of the MBLE using the Brooks–Corey model

Ref. [16] presented snapshots of the saturation profiles for different fluxes infiltrating into initially dry 20/30 sand. It's observed that for the highest ($v_T = 2.0 \times 10^{-3}$ [m s^{-1}]) and lowest ($v_T = 1.32 \times 10^{-7}$ [m s^{-1}]) fluxes the saturation profiles are monotonic with distance and no saturation overshoot is observed, while all of the intermediate fluxes ($v_T = 1.32 \times 10^{-3}$, 1.32×10^{-4}, 1.32×10^{-5}, 1.32×10^{-6} [m s^{-1}]) exhibit saturation overshoots. In this section we study the numerical solutions of (6) with flux function (7) and diffusion function (8). The physical parameters of the 20/30 sand [16,38] as well as the constants and the Brooks–Corey model [37] are listed in Table 6 and Table 7.

Remark. For realistic modeling of porous media flow, some researchers [5,10] also adopted the van Genuchten model. In Fig. 8 we plot $p_c(u)$, $H(u)$ and $H(u)p_c'(u)$ for both models. It's shown that although the Brooks–Corey capillary pressure has infinite derivative at $u = 0$ and the van Genuchten model involves infinite derivatives at $u = 0, 1$, the degeneracy of $H(u)$ makes $H(u)p_c'(u)$ degenerate at $u = 0, 1$. Therefore, we will not consider these extreme values. In the numerical simulations, when τ is large enough, we may get saturation overshoots above 1. Such results have also been observed for most extensions of Richards' equation [39,6]. In order to avoid overshoots above 1, Nieber et al. used a relaxation term of the

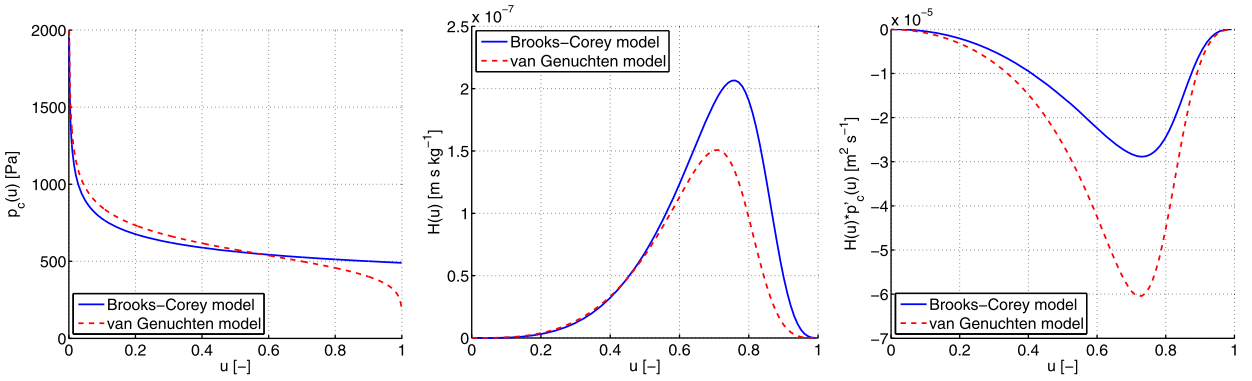

Fig. 8. Illustrations of $p_c(u)$, $H(u)$ and $H(u)p_c'(u)$ using Brooks–Corey model (parameters in imbibition process) and van Genuchten model ($p_c(u) = \frac{1}{\alpha}(u^{-\frac{1}{m}} - 1)^{\frac{1}{n}}$, $n = 6.23$, $m = 1 - \frac{1}{n}$, $\alpha = 1.8\text{e}{-3}$, parameters are from [16]).

Table 6
Physical parameters for 20/30 sand.

Sand	κ [m s^{-1}]	ϕ [–]	Drainage			Imbibition		
			u_{re} [–]	λ [–]	p_d [Pa]	u_{re} [–]	λ [–]	p_d [Pa]
20/30	2.5×10^{-3}	0.35	0	5.57	850	0	5	490

Table 7
Constants and the Brooks–Corey model.

Density [kg m^{-3}]	$\rho_w = 998.21$	$\rho_n = 1.2754$
Viscosity [kg m^{-1} s^{-1}]	$\mu_w = 1.002 \times 10^{-3}$	$\mu_n = 1.82 \times 10^{-5}$
Constants	$g = 9.81$ [m s^{-2}]	$K = \frac{\kappa \mu_w}{\rho_w g}$ [m^2]
	Capillary pressure	Relative permeability
Brooks–Corey model	$u_e = \frac{u - u_{re}}{1 - u_{re}}$	$k_{rw}(u) = u_e^{\frac{2+3\lambda}{\lambda}}$
	$p_c(u) = p_d u_e^{-\frac{1}{\lambda}}$, for $p_c > p_d$	$k_{rn}(u) = (1 - u_e)^2(1 - u_e^{\frac{2+\lambda}{\lambda}})$

form $\tau \sim p_c'(u)$ and a van Genuchten capillary pressure function in the dynamic relaxation model in [5]. Cueto-Felgueroso and Juanes [40] proposed a phase field model incorporated with an additional 'compressibility' term in the flow potential that constrains the water saturation to be between 0 and 1. In this paper, since we aim at solving the steep saturation front and the overshoot values, thus we will keep the model simple and avoid overshoots above 1 by choosing the parameters carefully instead of adding additional terms to restrict saturation.

Example 6. Full equation using the Brooks–Corey type model.

Using the physical parameters and the Brooks–Corey type model in Table 6 and Table 7, the flux $F(u)$ with different values of v_T and the diffusion function $H(u)$ are plotted in Fig. 9. The degeneracy of $H(u)$ at $u = 0$ introduces difficulty in the solving of (6), thus we should avoid using $u_0 = 0$. From Fig. 1 in Ref. [41] we get the initial capillary pressure $p_c^0 \approx 1600$ [Pa], when initial water saturation $u_0 = 0.003$, using parameters in the imbibition process we get the Brooks–Corey capillary pressure $p_c(u_0) = 1566$ [Pa]. Thus in the numerical simulations the initial saturation $u_0 = 0.003$ will be adopted. This initial saturation is also the measured value in Ref. [42].

Fig. 9 (left) shows that, the flux function $F(u)$ differs a lot for $v_T = 2.0 \times 10^{-3}, 1.32 \times 10^{-3}, 1.32 \times 10^{-4}$ [m s^{-1}]. Therefore, the bifurcation diagrams for these three cases are different from each other, see in Fig. 10. In order to simulate the saturation overshoot phenomenon, the dynamic coefficient τ has to be determined. We plot the τ–u pairs used in Ref. [12]. Notice that the τ–u pairs are beyond the scope of the bifurcation diagrams for $v_T = 2.0 \times 10^{-3}, 1.32 \times 10^{-3}$ and 1.32×10^{-4} [m s^{-1}]. Thus we have to choose new values of τ according to the bifurcation diagrams. For $v_T = 1.32 \times 10^{-3}, 1.32 \times 10^{-4}$ [m s^{-1}], let the corresponding plateau saturations $\bar{u}$ equal 0.98 and 0.95, by solving (17) and (18), the values of τ are 15.81 [Pa s^{-1}] and 1246 [Pa s^{-1}], respectively. The graphs of $w(u)$ are presented in Fig. 11 (left). Notice $w = -u_x$, in our numerical experiments such high values of $-u_x$ for $v_T = 1.32 \times 10^{-3}$ [m s^{-1}] can't be achieved using moving mesh method with $N \leq 800$ or uniform grid with $N \leq 4000$. In the following we will only consider $v_T = 1.32 \times 10^{-4}$ [m s^{-1}]. The bifurcations diagrams for $v_T = 1.32 \times 10^{-4}$ [m s^{-1}] with two different initial saturations $u_0 = 0.003$ and 0.03 are presented in Fig. 11 (right). Assuming that after a long time, the saturation at the left boundary reaches the equilibrium state, we set $\frac{\partial u}{\partial t}|_{x_l} = 0$, $\frac{\partial u}{\partial x}|_{x_l} = 0$. Then we obtain

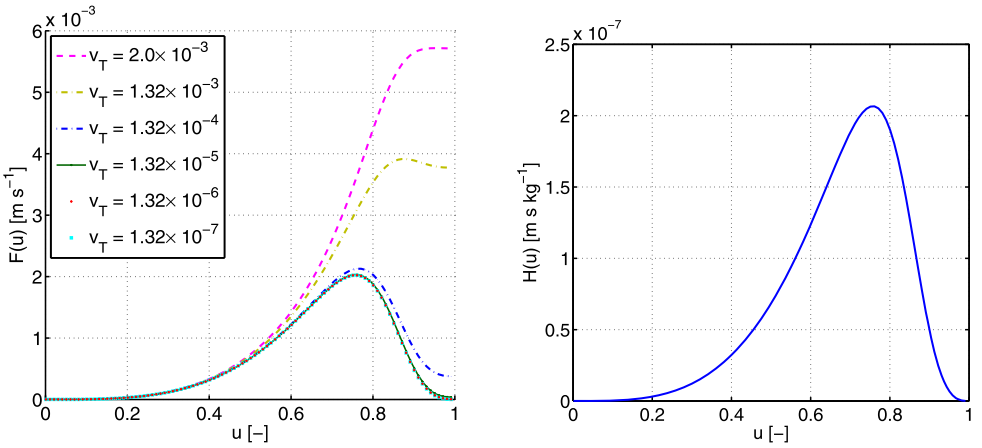

Fig. 9. The graphs of $F(u)$ for different values of v_T (left) and $H(u)$ (right).

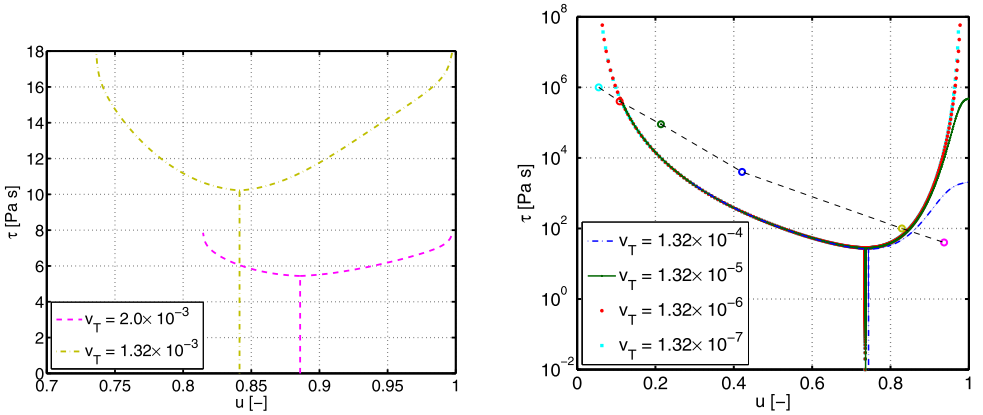

Fig. 10. The bifurcation diagrams for different values of v_T.

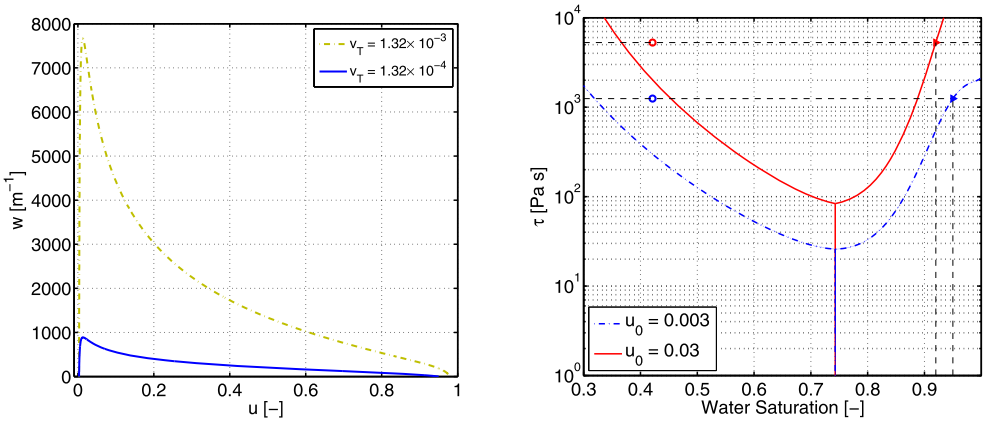

Fig. 11. Left: graphs of $w(u)$ with $v_T = 1.32 \times 10^{-3}$ and 1.32×10^{-4} [m s^{-1}]; Right: the bifurcation diagrams for initial saturation $u_0 = 0.003, 0.03$ with $v_T = 1.32 \times 10^{-4}$ [m s^{-1}].

$$v_T f(u) + \lambda_n(u) f(u)(\rho_w - \rho_n) g = v_T. \tag{46}$$

Solving (46) we get the boundary saturation u_B corresponding to v_T.

Using the initial condition

$$u(x, 0) = u_0 + 0.5(u_B - u_0)(1.0 - \tanh(200x)), \quad x \in [-0.05, 0.35], \tag{47}$$

Table 8
Traveling wave results for $u_0 = 0.003, 0.03$ with $v_T = 1.32 \times 10^{-4}$ [m s^{-1}].

u_0	u_B	τ [Pa s]	τ_* [Pa s]	τ_s [Pa s]	u_α	$\underline{u}$	$\bar{u}$	Wave description
0.003	0.4212	1246	25.89	2117	0.7440	0.3190	0.9500	Non-monotone plateau
0.03	0.4212	1246	83.52	368.4	0.7429	0.4533	0.8878	Non-monotone overshoot
0.03	0.4212	5271	83.52	588.9	0.7429	0.3664	0.9200	Non-monotone plateau

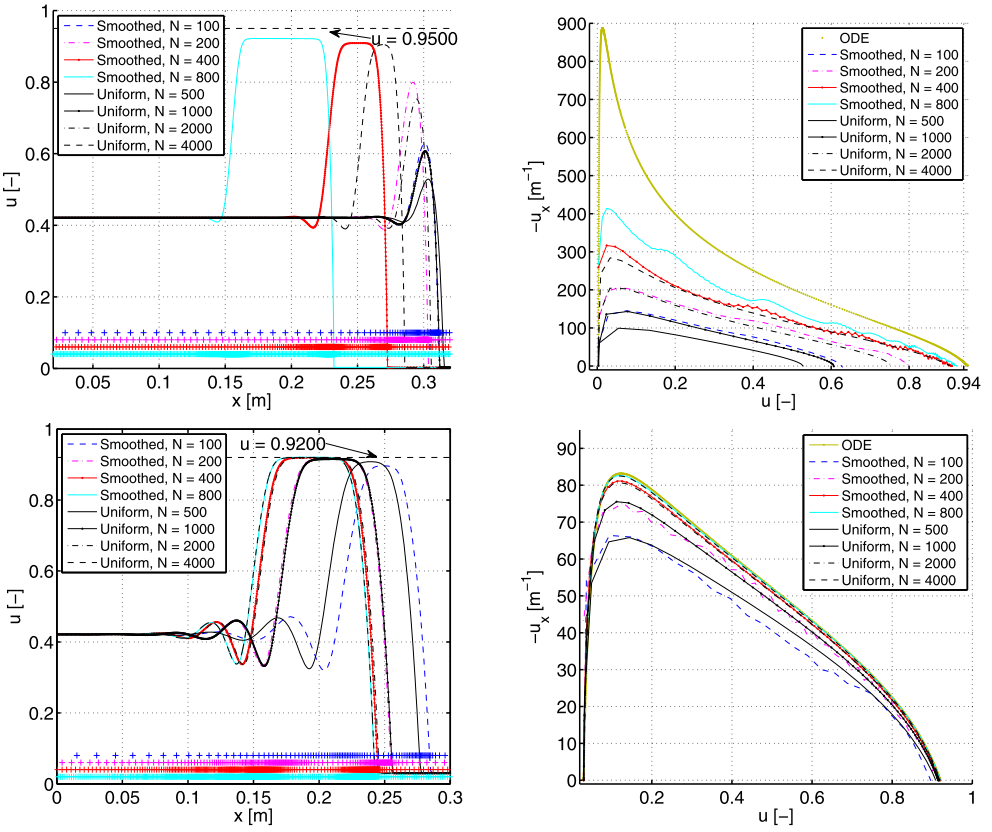

Fig. 12. Example 6: solutions (left) and values of $-u_x$ at the right boundary of the undercompressive shock (right) of the full model with $v_T = 1.32 \times 10^{-4}$ [m s^{-1}]. $u_0 = 0.003$ (top), $u_0 = 0.03$ (bottom).

the TW results obtained from Section 2.2 are listed in Table 8, the numerical results at $t = 350$ [s] are shown in Fig. 12. When $u_0 = 0.003$, it shows the more grid points we use, the more accurate is the plateau height. The uniform grid with $N = 4000$ only gives an overshoot which is lower than that of the moving mesh method with $N = 400$. The plateau height obtained by the moving mesh method with $N = 800$ is also lower than $\bar{u}$ in Table 8. This may be caused by the lack of grid points near the undercompressive shock: there are more grid points near the undercompressive shock for the moving mesh method than for the uniform grid, Fig. 12 (right) shows that the values of $-u_x$ obtained by the moving mesh method are higher than those using the uniform grids.

In Fig. 13 we compare the saturation profiles obtained by different values of $(u_0, \tau, t) = (0.003, 1246, 460)$, $(0.03, 1246, 350)$, $(0.03, 5271, 460)$ with the experimental results from Ref. [16]. When $u_0 = 0.03$ and $\tau = 1246$ [Pa s], Table 8 shows $u_B < \underline{u}$, $\tau > \tau_s$, thus instead of a plateau, the dynamic coefficient $\tau = 1246$ [Pa s] only gives an overshoot. When $u_0 = 0.03$ is fixed, a plateau is obtained using a higher value of $\tau = 5271$ [Pa s]. For $(u_0, \tau, t) = (0.03, 1246, 350)$ and $(0.03, 5271, 460)$, since $\tau > \tau_s$, oscillations appear near $u_B = 0.4212$. When $u_0 = 0.003$, the computed plateau height is $\bar{u}_c = 0.9214$, thus $\tau > \tau_{sc} = 614.5$ [Pa s], a small oscillation still exists near u_B. The plateau and tail saturations obtained with $(u_0, \tau, t) = (0.003, 1246, 460)$ are higher than the experimental values, we attribute this to the limitation of the Brooks–Corey model. Note that, the end time for $(u_0, \tau, t) = (0.003, 1246, 460)$ is very near to the calculated end time $t = 409.7$ [s] in Ref. [12], this validates the accuracy of our approach.

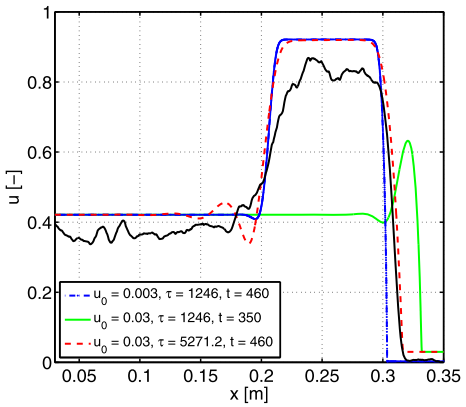

Fig. 13. Comparisons between experimental result and numerical solutions obtained for $(u_0, \tau, t) = (0.003, 1246, 460)$, $(0.03, 1246, 350)$, $(0.03, 5271, 460)$ using moving mesh method with $N = 800$.

5. Conclusions

In this paper we applied an adaptive moving mesh technique to solve the two-phase flow equation in porous media incorporating the dynamic capillary pressure term. The moving mesh method successfully captured the monotone and non-monotone solutions with high accuracy. Comparisons between numerical results show that to achieve the same accuracy, the moving mesh method needs approximately a factor of 5–10 fewer grid points than the uniform case. The computed saturation profiles and grid trajectories also illustrate different features of the smoothed monitor function and the arc-length monitor function. The arc-length monitor function have higher accuracy in steep regions, while the smoothed monitor function gives a better balance between the smooth and the steep regions.

Acknowledgements

The research of H. Zhang was funded by the China Scholarship Council (No. 201503170430). The authors would like to thank Prof. Iuliu Sorin Pop for providing code to compute the values of τ in this paper and Prof. David DiCarlo for providing the experimental profiles from [16]. Moreover, the valuable suggestions from the anonymous referees are highly appreciated.

References

[1] G. Barenblatt, Filtration of two nonmixing fluids in a homogeneous porous medium, Fluid Dyn. 6 (5) (1971) 857–864.
[2] F. Stauffer, Time dependence of the relations between capillary pressure, water content and conductivity during drainage of porous media, in: IAHR Symposium on Scale Effects in Porous Media, Thessaloniki, Greece, vol. 29, 1978, pp. 3–35.
[3] S.M. Hassanizadeh, W.G. Gray, Thermodynamic basis of capillary pressure in porous media, Water Resour. Res. 29 (10) (1993) 3389–3405.
[4] S.M. Hassanizadeh, M.A. Celia, H.K. Dahle, Dynamic effect in the capillary pressure–saturation relationship and its impacts on unsaturated flow, Vadose Zone J. 1 (1) (2002) 38–57.
[5] J.L. Nieber, R.Z. Dautov, A.G. Egorov, A.Y. Sheshukov, Dynamic capillary pressure mechanism for instability in gravity-driven flows; review and extension to very dry conditions, Transp. Porous Media 58 (1–2) (2005) 147–172.
[6] D.A. DiCarlo, Modeling observed saturation overshoot with continuum additions to standard unsaturated theory, Adv. Water Resour. 28 (10) (2005) 1021–1027.
[7] C. Van Duijn, L. Peletier, I. Pop, A new class of entropy solutions of the Buckley–Leverett equation, SIAM J. Math. Anal. 39 (2) (2007) 507–536.
[8] A. Mikelić, A global existence result for the equations describing unsaturated flow in porous media with dynamic capillary pressure, J. Differ. Equ. 248 (6) (2010) 1561–1577.
[9] K. Spayd, M. Shearer, The Buckley–Leverett equation with dynamic capillary pressure, SIAM J. Appl. Math. 71 (4) (2011) 1088–1108.
[10] G. Sander, O. Glidewell, J. Norbury, Dynamic capillary pressure, hysteresis and gravity-driven fingering in porous media, J. Phys. Conf. Ser. 138 (2008) 012023, IOP Publishing.
[11] M. Chapwanya, J.M. Stockie, Numerical simulations of gravity-driven fingering in unsaturated porous media using a nonequilibrium model, Water Resour. Res. 46 (9) (2010) W09534.
[12] H. Zhang, P.A. Zegeling, A numerical study of two-phase flow models with dynamic capillary pressure and hysteresis, Transp. Porous Media 116 (2) (2017) 825–846.
[13] R.J. Glass, T.S. Steenhuis, J.-Y. Parlange, Mechanism for finger persistence in homogeneous, unsaturated, porous media: theory and verification, Soil Sci. 148 (1) (1989) 60–70.
[14] J. Selker, J.-Y. Parlange, T. Steenhuis, Fingered flow in two dimensions: 2. Predicting finger moisture profile, Water Resour. Res. 28 (9) (1992) 2523–2528.
[15] Y. Liu, T.S. Steenhuis, J.-Y. Parlange, Formation and persistence of fingered flow fields in coarse grained soils under different moisture contents, J. Hydrol. 159 (1–4) (1994) 187–195.
[16] D.A. DiCarlo, Experimental measurements of saturation overshoot on infiltration, Water Resour. Res. 40 (4) (2004) W04215.
[17] C. Cuesta, C. Van Duijn, J. Hulshof, Infiltration in porous media with dynamic capillary pressure: travelling waves, Eur. J. Appl. Math. 11 (04) (2000) 381–397.
[18] C. Van Duijn, Y. Fan, L. Peletier, I.S. Pop, Travelling wave solutions for degenerate pseudo-parabolic equations modelling two-phase flow in porous media, Nonlinear Anal., Real World Appl. 14 (3) (2013) 1361–1383.

[19] X. Cao, I. Pop, Uniqueness of weak solutions for a pseudo-parabolic equation modeling two phase flow in porous media, Appl. Math. Lett. 46 (2015) 25–30.
[20] M. Peszynska, S.-Y. Yi, Numerical methods for unsaturated flow with dynamic capillary pressure in heterogeneous porous media, Int. J. Numer. Anal. Model. 5 (Special Issue) (2008) 126–149.
[21] Y. Wang, C.-Y. Kao, Central schemes for the modified Buckley–Leverett equation, J. Comput. Sci. 4 (1) (2013) 12–23.
[22] C.-Y. Kao, A. Kurganov, Z. Qu, Y. Wang, A fast explicit operator splitting method for modified Buckley–Leverett equations, J. Sci. Comput. 64 (3) (2015) 837–857.
[23] P.A. Zegeling, An adaptive grid method for a non-equilibrium PDE model from porous media, J. Math. Study 48 (2) (2015) 187–198.
[24] F. Doster, P. Zegeling, R. Hilfer, Numerical solutions of a generalized theory for macroscopic capillarity, Phys. Rev. E 81 (3) (2010) 036307.
[25] G. Hu, P.A. Zegeling, Simulating finger phenomena in porous media with a moving finite element method, J. Comput. Phys. 230 (8) (2011) 3249–3263.
[26] H. Dong, Z. Qiao, S. Sun, T. Tang, Adaptive moving grid methods for two-phase flow in porous media, J. Comput. Appl. Math. 265 (2014) 139–150.
[27] F. Kalaydjian, A macroscopic description of multiphase flow in porous media involving spacetime evolution of fluid/fluid interface, Transp. Porous Media 2 (6) (1987) 537–552.
[28] C. Cuesta, C. van Duijn, I. Pop, Non-classical shocks for Buckley–Leverett: degenerate pseudo-parabolic regularisation, in: Progress in Industrial Mathematics at ECMI 2004, Springer, 2006, pp. 569–573.
[29] P. Zegeling, Theory and application of adaptive moving grid methods, in: Adaptive Computations: Theory and Algorithms, 2007, pp. 279–332.
[30] W. Huang, R.D. Russell, Analysis of moving mesh partial differential equations with spatial smoothing, SIAM J. Numer. Anal. 34 (3) (1997) 1106–1126.
[31] W. Huang, Y. Ren, R.D. Russell, Moving mesh partial differential equations (MMPDEs) based on the equidistribution principle, SIAM J. Numer. Anal. 31 (3) (1994) 709–730.
[32] W. Huang, W. Sun, Variational mesh adaptation II: error estimates and monitor functions, J. Comput. Phys. 184 (2) (2003) 619–648.
[33] P. Zegeling, W. De Boer, H. Tang, Robust and efficient adaptive moving mesh solution of the 2-D Euler equations, Contemp. Math. 383 (2005) 419–430.
[34] A. Van Dam, P. Zegeling, Balanced monitoring of flow phenomena in moving mesh methods, Commun. Comput. Phys. 7 (1) (2010) 138–170.
[35] W. Huang, Practical aspects of formulation and solution of moving mesh partial differential equations, J. Comput. Phys. 171 (2) (2001) 753–775.
[36] MATLAB, version 8.3.0.532 (R2014a), The Mathworks, Inc., Natick, Massachusetts, 2014.
[37] R.H. Brooks, A. Corey, Properties of porous media affecting fluid flow, J. Irrig. Drain. Div. 92 (2) (1966) 61–90.
[38] M. Schroth, J. Istok, S. Ahearn, J. Selker, Characterization of miller-similar silica sands for laboratory hydrologic studies, Soil Sci. Soc. Am. J. 60 (5) (1996) 1331–1339.
[39] M. Eliassi, R.J. Glass, On the porous continuum-scale modeling of gravity-driven fingers in unsaturated materials: numerical solution of a hypodiffusive governing equation that incorporates a hold-back-pile-up effect, Water Resour. Res. 39 (6) (2003) 1167.
[40] L. Cueto-Felgueroso, R. Juanes, A phase field model of unsaturated flow, Water Resour. Res. 45 (10) (2009) W10409.
[41] D.A. DiCarlo, Capillary pressure overshoot as a function of imbibition flux and initial water content, Water Resour. Res. 43 (8) (2007) (online).
[42] T. Yao, J. Hendrickx, Stability analysis of the unsaturated water flow equation: 2. Experimental verification, Water Resour. Res. 37 (7) (2001) 1875–1881.